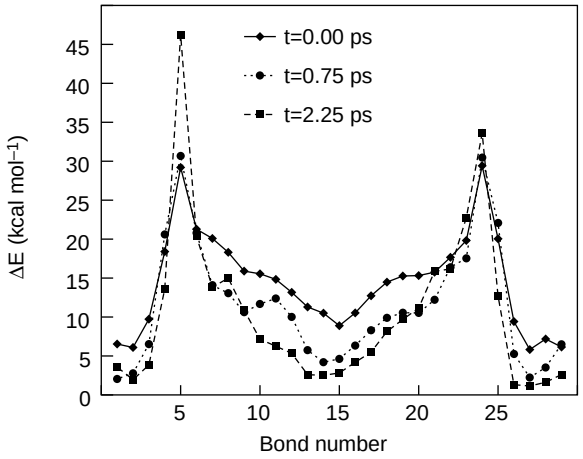

Figure 4 Relaxation of the strain energy distribution. Shown is the distribution along a $C_{30}H_{62}$ chain containing a trefoil during CPMD energy minimization at $T = 0$ K. The $t = 0$ configuration is an average of the equilibrium positions obtained from classical MD simulations performed with different initial states and temperatures. The segments outside the knot and its central portion relax, while stress tends to concentrate mostly on the two entrance bonds (see Fig. 1).

after which it was cooled. Typically, during the dynamical evolution individual bonds undergo large-amplitude thermal fluctuations, which decrease on cooling.

During the room temperature $L = 13.50$ Å CPMD run for $N = 28$, dissociation occurred at a bond location just outside the entrance to the knot, well separated from the terminal atom where the tension was applied. Figure 2 shows the region of the knot where the chain actually ruptured, both before (Fig. 2a) and after (Fig. 2b) the break. The change in hybridization of the C_{22} and C_{23} atoms from sp^3 to sp^2 is clearly evident also in Fig. 2c, where we display the time evolution of the system immediately before and after the break. Figure 3 shows a 'snapshot' of the electronic charge density after the break occurred. The gap in the charge density between the C_{22} and C_{23} atoms confirms the bond breaking at this position. Other simulations carried out with $L \geq 13.50$ Å yield breakpoints at one of the two bonds coming out from the knot. (Density-functional energy barriers are not quantitatively very accurate, but the general qualitative description of phenomena, as well as the dissociation energies involved in such processes, are known to be quite reliable.)

The first-principles CPMD calculations provide the total strain energy but not its profile along the chain. The latter can be obtained by making use of an *ab initio* force-constants model, which is able to reproduce the total strain energy to ~20%. Figure 4 shows the evolution of the strain energy distribution during structural relaxation of a $N = 30$ trefoil just before breaking occurs. The strain energy is mainly localized in the two symmetric bonds that are outside the entrance to the knot. Our calculations suggest that 23 carbon atoms form the tightest knot that can be sustained in a polyethylene strand without it breaking.

The strain energy stored in the knot at breaking point is 12.7 kcal mol^{-1} per C–C bond, which is considerably smaller than the value (16.2 kcal mol^{-1}) for the linear unknotted case. Thus, we find that the presence of the knot has significantly weakened the strand in which it is tied.

Although the dynamical evolution of the present constrained *ab initio* MD simulations was sufficient to observe bond breaking, no attempt was made to allow for recombination of the resulting radicals or reactions of the radicals with other parts of the chain. The study of these effects, as well as the role of chain branching and the influence of neighbouring chains, is left for future research. These factors will probably provide a deeper understanding of how the interplay between inter- and intra-molecular effects contributes to the mechanical properties of real polymer samples[2].

Note added in proof: Arai *et al.*[26] have recently reported the knotting of actin filaments and DNA molecules using optical tweezers. They find that the breaking stress for actin is significantly lower than that of the unknotted filaments, and that the breakage point is at the entrance to the knot, as our calculations predict. □

Received 22 September 1998; accepted 22 February 1999.

1. Ashley, C. W. *The Ashley Book of Knots* (Doubleday, New York, 1993).
2. Bayer, R. K. Structure transfer from a polymeric melt to the solid state. Part III: Influence of knots on structure and mechanical properties of semicrystalline polymers. *Colloid Polym. Sci.* **272,** 910–932 (1994).
3. Atiyha, M. F. *The Geometry and Physics of Knots* (Cambridge Univ. Press, 1990).
4. Katritch, V. *et al.* Geometry and physics of knots. *Nature* **383,** 142–145 (1996); Properties of ideal composite knots. *Nature* **388,** 148–151 (1997).
5. Frisch, H. L. & Wasserman, E. Chemical topology, *J. Am. Chem. Soc.* **83,** 3789–3795 (1961).
6. Mislow, K. *Introduction to Stereochemistry* (Benjamin, New York, 1965).
7. Schill, G. *Catenanes, Rotaxanes, and Knots* (Academic, New York, 1971).
8. Walba, D. M. Topological stereochemistry. *Tetrahedron* **41,** 3161–3212 (1985).
9. Frank-Kamenetskii, M. D., Lukashin, A. V. & Vologodskii, A. V. Statistical mechanics and topology of polymer chains. *Nature* **258,** 398–402 (1975).
10. Frisch, H. L. Macromolecular topology—Metastable isomers from pseudo interpenetrating polymer networks. *New J. Chem.* **17,** 697–701 (1993).
11. Mansfield, M. L. Knots in hamiltonian cycles. *Macromolecules* **27,** 5924–5926 (1994).
12. van Rensburg, E. J., Sumners, D. A. W., Wasserman, E. & Whittington, S. G. Entanglement complexity of self-avoiding walks. *J. Phys. A* **25,** 6557–6566 (1992).
13. Wasserman, S. A. & Cozzarelli, N. R. Biochemical topology: applications to DNA recombination and replication. *Science* **232,** 951–960 (1986).
14. Shaw, S. Y. & Wang, J. C. Knotting of a DNA chain during ring closure. *Science* **260,** 533–536 (1993).
15. Schlick, T. & Olson, W. K. Trefoil knotting revealed by molecular dynamics simulations of supercoiled DNA. *Science* **257,** 1110–1115 (1992).
16. Car, R. & Parrinello, M. Unified approach for molecular dynamics and density-functional theory. *Phys. Rev. Lett.* **55,** 2471–2474 (1985).
17. de Gennes, P.-G. Tight knots. *Macromolecules* **17,** 703–704 (1984).
18. Siepmann, J. I., Karaborni, S. & Smit, B. Simulating the critical-behaviour of complex fluids. *Nature* **365,** 330–332 (1993).
19. Mundy, C. J., Balasubramanian, S., Bagchi, K., Siepmann, J. I. & Klein, M. L. Equilibrium and non-equilibrium simulation studies of fluid alkanes in bulk and at interfaces. *Faraday Discuss.* **104,** 17–36 (1996).
20. Karasawa, N., Dasgupta, S. & Goddard, W. A. Mechanical properties and force-field parameters for polyethylene crystal. *J. Phys. Chem. US* **95,** 2260–2272 (1991).
21. Ancilotto, F., Chiarotti, G. L., Scandolo, S. & Tosatti, E. Dissociation of methane into hydrocarbons at extreme (planetary) pressure and temperature. *Science* **275,** 1288–1290 (1997).
22. Montanari, B. & Jones, R. O. Density functional study of crystalline polyethylene. *Chem. Phys. Lett.* **272,** 347–352 (1997).
23. Martyna, G. J. *et al.* PINY Code. *Comp. Phys. Comm.* (in the press).
24. Becke, A. D. Density-functional exchange-energy approximation with correct asymptotic behavior. *Phys. Rev. A* **38,** 3098–3100 (1988).
25. Lee, C., Chang, W. & Parr, R. G. Development of the Colle-Salvetti correlation-energy formula into a functional of the electron density. *Phys. Rev. B* **37,** 785–789 (1988).
26. Arai, Y. *et al.* Tying a molecular knot with optical tweezers. *Nature* (in the press).

Acknowledgements. This work was supported in part by the National Science Foundation.

Correspondence and requests for material should be addressed to M.L.K. (e-mail: klein@lrsm.upenn. edu).

Controlled growth and electrical properties of heterojunctions of carbon nanotubes and silicon nanowires

Jiangtao Hu*†, Min Ouyang*†, Peidong Yang‡ & Charles M. Lieber*§

* *Department of Chemistry and Chemical Biology, Harvard University, Cambridge, Massachusetts 02138, USA*
‡ *Department of Chemistry, University of California, Santa Barbara, California 93106, USA*
§ *Division of Engineering and Applied Science, Harvard University, Cambridge, Massachusetts 02138, USA*
† *These authors contributed equally to this work.*

Nanometre-scale electronic structures are of both fundamental and technological interest: they provide a link between molecular and solid state physics, and have the potential to reach far higher

device densities than is possible with conventional semiconductor technology[1,2]. Examples of such structures include quantum dots, which can function as single-electron transistors[3,4] (although their sensitivity to individual stray charges might make them unsuitable for large-scale devices) and semiconducting carbon nanotubes several hundred nanometres in length, which have been used to create a field-effect transistor[5]. Much smaller devices could be made by joining two nanotubes or nanowires to create, for example, metal–semiconductor junctions, in which the junction area would be about 1 nm^2 for single-walled carbon nanotubes. Electrical measurements of nanotube 'mats' have shown the behaviour expected for a metal–semiconductor junction[6]. However, proposed nanotube junction structures[7] have not been explicitly observed, nor have methods been developed to prepare them. Here we report controlled, catalytic growth of metal–semiconductor junctions between carbon nanotubes and silicon nanowires, and show that these junctions exhibit reproducible rectifying behaviour.

Two approaches were used to prepare nanotube–nanowire (NT/NW) junctions (Fig. 1). These methods built on recent efforts in our group[8] and elsewhere[9,10] directed towards the controlled growth of NWs and NTs with catalysts. It is possible to extend the basic ideas from this previous work to create NT/NW junctions by localizing a suitable metal catalyst at the end of a starting NW or NT. We have met this critical requirement by using a common catalyst for the growth of the NW and NT, and by depositing a NW catalyst at the end of an existing NT.

A common Fe-based catalyst was used to grow NTs from the ends of silicon NWs (SiNWs). In previous work, we have shown that Fe and Fe/Au are efficient catalysts for the growth of SiNWs[8]; moreover, it is well established that Fe is a good catalyst for the growth of multiwalled NTs (MWNTs)[9] and single-walled NTs (SWNTs)[10]. The use of a common catalyst has the advantage that the catalyst is naturally localized at the ends of the SiNWs after their growth, and then can be used to direct the growth of NTs using a hydrocarbon reactant such as ethylene (Fig. 1a). The SiNWs grown with Fe/Au catalysts are single-crystal materials with an average diameter of ~10 nm (Fig. 2a). Transmission electron microscopy (TEM) and X-ray fluorescence (EDX) analyses further demonstrate that the SiNWs terminate in well-defined Fe/Au nanoclusters.

NTs were grown from the ends of the SiNWs by using ethylene at 600 °C. TEM studies of the products produced in this way show a large number of NT/SiNW junctions (for example, Figs 2b, c), where NTs are clearly hollow and SiNWs are solid. Electron diffraction (Fig. 2b, inset) and high-resolution imaging reveal that the SiNWs remain crystalline after NT growth. The observed NT wall thicknesses and lattice-resolved imaging demonstrate that the NTs are well-ordered MWNTs as expected for these growth conditions[9]. We find that two general junction structures are produced from the SiNW ends. In the more common case, the NT forms a sharp junction with the SiNW (Fig. 2b). A metal nanocluster, which can be excluded during growth, is often observed nearby the junction. Because MWNTs are typically metallic[11], these sharp NT/SiNW nanojunctions can exhibit behaviour typical of metal–semiconductor (M/S) junctions formed on planar silicon[12]. In the second less frequent type of junction, a catalyst cluster remains in the region between the NT and SiNW (Fig. 2c, large arrow). This latter image also exhibits contrast changes in the SiNW portion of the junction. EDX and electron diffraction measurements demonstrate that these regions do not contain significant metal catalyst

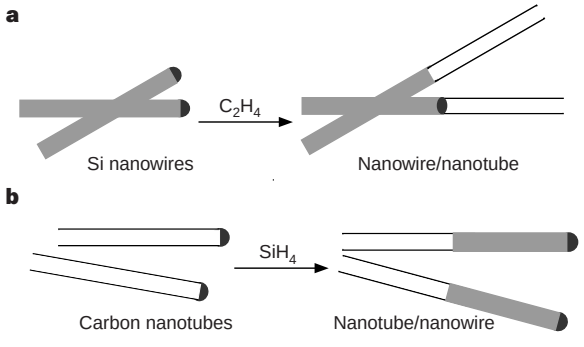

Figure 1 Synthetic approaches to NT/SiNW junctions. **a**, SiNWs (grey) grown by a catalytic process[8] terminate in nanocluster catalysts (black). This catalyst is used to direct the growth of NTs (black lines) from ethylene. The catalyst can be excluded or remain at the NT/SiNW junction. **b**, Catalyst nanoclusters (black) are deposited on NT ends and then used to direct the growth of SiNWs. In this case, the catalyst is on the SiNW free end and the NT/SiNW junction is clean.

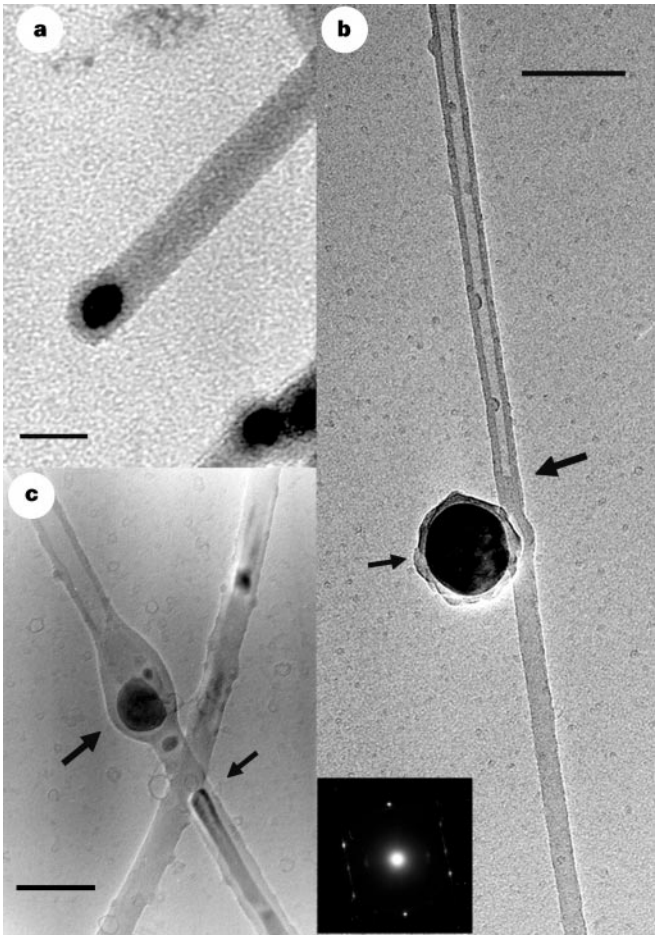

Figure 2 NT/SiNW junctions grown from SiNWs with a common Fe/Au catalyst. **a**, TEM image (EM420; Philips) of SiNW produced with a $Fe_{0.9}Au_{0.1}$ catalyst. The 15-nm-diameter NW terminates in a Fe–Au nanocluster that appears as a dark, solid sphere. **b**, **c**, TEM images of NT/SiNW junctions. The hollow NTs are oriented at the top of both images and the solid SiNWs at the bottom. **b**, The large black arrow highlights the junction position. The small arrow indicates a metal catalyst cluster that was probably excluded from the junction during growth. The inset corresponds to an electron diffraction pattern recorded with the beam perpendicular to the NT/SiNW axis. The diffraction spots show that the SiNW maintains its crystalline structure after NT growth. **c**, The larger arrow highlights the junction region that contains a metal nanocluster. The contrast variation highlighted by the smaller arrow corresponds to SiNW (see the text for details). The scale bars in **a**, **b** and **c** are 20, 50 and 50 nm, respectively. Samples were prepared as follows. A pulsed Nd–YAG laser (532 nm, 7-ns pulse width; GCR-16S; Spectra-Physics) was used to ablate a $Fe_{0.9}Au_{0.1}$ solid target placed within a growth system[8]. The ablation was performed for 10 min in 20-torr 10%/90% silane/He (99.998%; Matheson Gas Products), 20 standard cm^3 min^{-1} at 450 °C. NTs were grown from the SiNWs for 30 min in 300-torr ethylene (99.5%; Matheson Gas Products), 20 standard cm^3 min^{-1} at 600 °C.

and are crystalline Si. We believe that the contrast changes are due to Si recrystallization and texturing mediated by Au(Fe) catalyst during NT growth. This type of junction is more complex than the more common sharp NT/SiNW structure but should also exhibit M/S behaviour, as both the NT and catalyst particles are metallic.

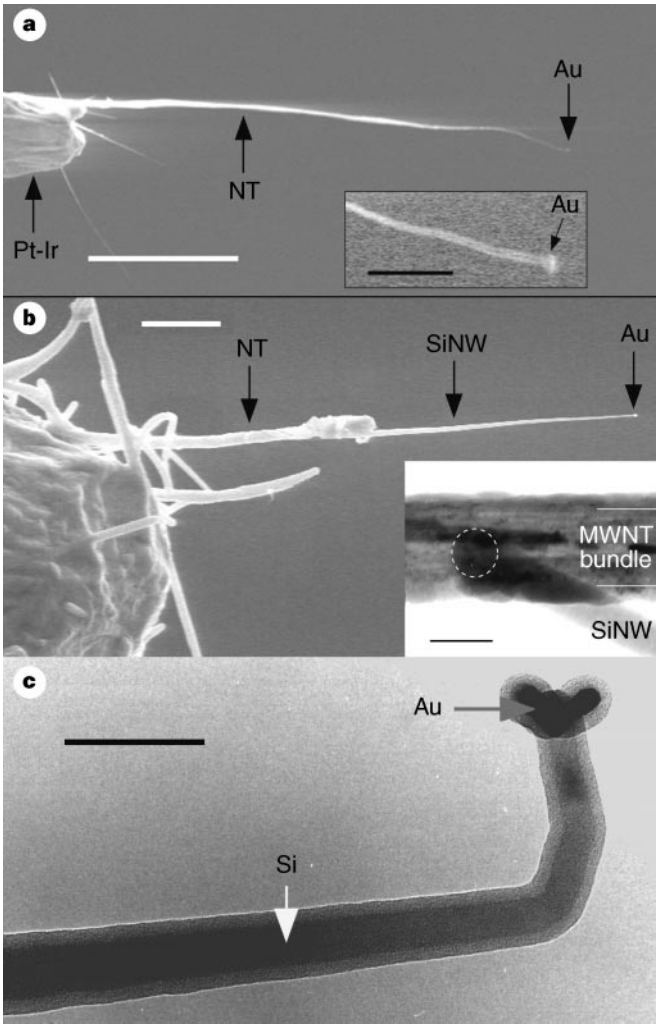

Figure 3 NT/SiNW junctions grown from NT tips with a Au catalyst. **a**, FESEM images (Leo 982; Leo Electron Microscopy) of a NT with an electrodeposited Au nanocluster at the free end. The NT is attached to a Pt–Ir STM tip with micromanipulators[13]. Inset, higher-magnification view of the Au nanocluster at the NT end. The apparent doubling of the NT is due to vibration of the long tube. The white and black scale bars correspond to 5 μm and 500 nm, respectively. **b**, FESEM image of the NT/SiNW junction grown from a nanotube tip. The large structure at the left is the Pt–Ir tip; several spurious nanotubes are present on the tip surface from the initial transfer process. Scale bar, 2 μm. Inset, TEM image of a NT/SiNW junction. The junction, which is indicated by the dashed white circle, is located at the back of the MWNT bundle and seems clean (for example, there is no evidence for Au in the image). The extent of the MWNT bundle is indicated with white lines; amorphous Si/SiO_x covers the surface as described in the text. Scale bar, 50 nm. **c**, TEM image of the tip of the nanowire in **b**. The nanowire consists of a crystalline core and an amorphous Si/SiO_x coating. Diffraction and EDX studies demonstrate that there is undetectable (<0.5%) gold in the nanowire and NT/SiNW junction, and that there is a well-defined Au nanocluster at the SiNW free end. Scale bar, 50 nm. Samples were prepared as follows. MWNTs[18] were mounted onto freshly cut Pt–Ir STM tips with silver paste (H20E; Epoxy Technology), and gold nanoclusters were electroplated on the free NT ends (Techni-Gold 25 E; Technic) at 500 mV. SiNWs were then grown from the NT ends by chemical vapour deposition (CVD) (10%/90% silane/He, 20 standard $cm^3\,min^{-1}$ for 15 min at 510 °C).

We have also studied growth from catalysts attached to NTs. This method provides greater flexibility in the choice of catalyst and enables direct electrical measurements, as NTs can be easily attached to scanned probe microscopy tips[13]. NTs were attached to sharpened Pt–Ir STM tips, and then a gold cluster was electrodeposited onto the NT free ends. Typical field-emission scanning electron microscope (FESEM) images of an attached MWNT bundle show that it is possible to localize Au nanoclusters at the very end of NT tips (Fig. 3a). The apparent splitting in the high-resolution image (Fig. 3a, inset) is due to the vibration of the long NT.

To create NT/SiNW junctions, SiNWs were grown from the NT tip ends by using silane[14]. A typical FESEM image of a NT/SiNW junction (Fig. 3b) shows roughly equal 5 μm straight segments of NT and SiNW with the junction near the centre of the image. TEM and FESEM images of the SiNW portion of the structure further demonstrate (1) that the NWs consist of a crystalline Si core sheathed in a thin, amorphous Si (α-Si) and native SiO_x layer (which forms after the sample is exposed to air), (2) that the Au catalyst used to direct growth is at the SiNW end (Fig. 3c), and (3) that the nanotube and SiNW can be either on-axis (Fig. 3b) or off-axis (Figs 3b and 4a, insets). TEM and EDX also demonstrate that the NT/SiNW structures prepared in this way do not have detectable Au, α-Si or SiO_x at the junction interface (Fig. 3b, inset). We believe that the preference for growth with Au catalyst at the SiNW free end reflects the more favourable energetics of NT–solid Si versus NT–liquid Au/Si interfaces.

There are two other features of the NT/SiNW junctions produced by this latter method that are evident in Fig. 3. First, the NT diameters are larger after SiNW growth. This reflects the uncata-

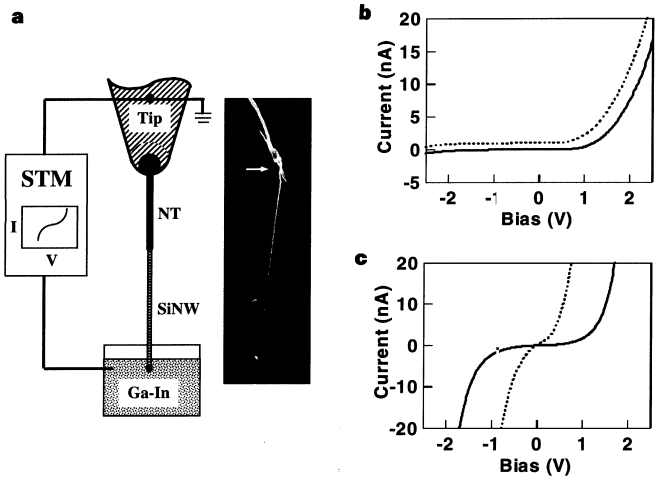

Figure 4 Electrical properties of NT/SiNW junctions. **a**, Diagram of the set-up used to measure the electrical properties of nanojunctions. The NT/SiNW is electrically connected to a Pt–Ir tip with Ag paste at the NT end (filled black circle) and to Ga–In liquid metal at the SiNW end. *I–V* curves are measured with the scanning tunnelling microscope (STM) electronics. Inset, another NT/SiNW junction grown as described in Fig. 3. The arrow indicates the position of the junction with the NT and SiNW above and below this point, respectively. **b**, *I–V* curves of two independent NT/SiNW junctions (solid and dotted curves). The reverse bias region of the dotted curve overlaps the solid curve and was shifted for clarity. **c**, *I–V* curves of a NT (dotted), coated with a thin layer of amorphous silicon, and a SiNW (solid) connected directly to the Pt–Ir tip. The current through SiNWs was 3–5 times that through NT/SiNW junctions over the voltage range used to determine ϕ_b. This shows that forward bias response of the NT/SiNW structures is dominated by the internal junction. Experimental procedures were as follows. Pt–Ir tips with NT/NW junctions were mounted in a commercial STM (Nanoscope III; Digital Instruments) equipped with a variable-gain current amplifier (QME 311; Balzers). The NT/SiNW junctions were advanced or retracted in 25 nm steps into or from the Ga–In liquid (99.99%; Alfa Aesar), with the STM feedback loop disabled; *I–V* measurements were made at a variety of depths.

lysed deposition of α-Si (from silane) during NW growth. Second, many of the SiNWs grown on NTs with the Au catalyst seem to taper towards the end. A reduction in diameter with increasing length has been reported previously for larger Si whiskers; this reduction was attributed to the incorporation of gold in the Si phase during growth[14]. Although we do not have direct evidence for Au-doping of the SiNWs, it should be noted that Au is expected to create deep acceptor and donor levels in Si (ref. 15) that are electrically inactive.

We have measured directly the electrical properties of individual NT/SiNW junctions grown from NT tips with an approach that exploits a liquid metal[16] to make the second electrical contact to the free ends of NT/SiNW junctions (Fig. 4a). The current–voltage (I–V) measurements on NT/SiNW junctions with only the SiNW in contact with the Ga–In liquid exhibit very reproducible rectifying behaviour typified by the results for two independent junctions shown in Fig. 4b. Specifically, there is little current flow for $V < 0$, whereas the current increases sharply for voltages $\gtrsim$+0.8. Similar results were obtained in nine independent nanojunctions. Significantly, this rectifying behaviour is characteristic of a M/S Schottky diode device.

Several experiments lead us to conclude that this diode-like behaviour is intrinsic to the nanoscale NT/SiNW junctions. First, I–V curves remain unchanged as the tip is advanced into the Ga–In liquid as long as this distance does not exceed the measured length of the SiNW. These results suggest that the overall current flow is limited by the actual NT/SiNW junction. Second, when the tips are advanced past the SiNW so that the NT is in contact with Ga–In liquid, symmetrical, non-rectifying I–V curves are observed (Fig. 4c). These results show that the NT/Pt–Ir junction does not produce the observed diode characteristics. The non-ohmic I–V curves recorded when the NT is in contact with Ga–In are due to the barrier created by the thin α-Si/SiO_x coating formed on the NT during NW growth and subsequent exposure to air (see above). Third, I–V measurements made on SiNWs grown directly from the Pt–Ir tips (the same conditions as for NT/SiNW growth) are symmetrical, exhibit no evidence of rectifying behaviour but have characteristics of a tunnel junction (Fig. 4c). These results demonstrate that the observed diode behaviour is not due to the SiNW/Ga–In contact or a Si/α–Si interface. We believe that the SiNW/Ga–In contact is a tunnel junction due to the native surface oxide layer[12], whereas the SiNW/Pt contact is ohmic, as observed previously for p-Si/Pt junctions[17]. Last, the nine independent NT/SiNW junctions that we have synthesized all exhibit the well-defined rectifying behaviour shown in Fig. 4b, thus testifying to the reproducibility of these nanojunctions.

The NT/SiNW M/S junctions exhibit Schottky diode behaviour similar to much larger planar Si-based structures, despite their small size. To explore the similarity further we have analysed the forward bias I–V data to extract the zero-bias junction barrier height, ϕ_b (ref. 12). It is interesting that this provides values of ϕ_b, 0.41 ± 0.06 eV, very similar to those obtained for macroscopic metal/p-Si junctions[12], in which we have verified that the SiNWs are p-doped (J.H., M.O. and C.M.L., unpublished observations).

Our controlled synthesis of NT/SiNW M/S junctions exhibiting Schottky diode behaviour opens up exciting opportunities on several fronts. They show that conventional semiconductor device structures of very small junction area can be embedded within NT/NW structures and that these quantum wires can serve as a natural means for electrically addressing the nanojunctions. Further studies of these structures, for example as a function of NW/NT diameter and temperature, will provide insight into the nanojunction physics and enable minimum size limits to be defined. More generally, we believe that the catalytic approach used to prepare NT/SiNW junctions can be readily expanded to create other M/S and semiconductor–semiconductor structures. Formation of junctions between p-type and n-type semiconductors could produce remarkably small light-emitting diodes that could also be readily addressed electrically. It is therefore reasonable to speculate that nanojunctions formed by the method described here could provide some of the critical building blocks needed to enable the emerging technology of nanoelectronics. □

Received 23 November 1998; accepted 1 March 1999.

1. Carter, F. L. *Molecular Electronic Devices* (Marcel Dekker, New York, 1982).
2. Timp, G. *Nanoscience and Technology* (AIP Press, New York, in the press).
3. Devoret, M. H., Esteve, D. & Urbina, C. Single-electron transfer in metallic nanostructures. *Nature* **360,** 547–553 (1992).
4. Klein, D. L., Roth, R., Lim, A. K. L., Alivisator, A. P. & McEuen, P. L. A single-electron transistor made from a cadmium selenide nanocrystal. *Nature* **389,** 699–701 (1997).
5. Tans, S. J., Verschueren, A. R. M. & Dekker, C. Room-temperature transistor based on a single carbon nanotube. *Nature* **393,** 49–52 (1998).
6. Collins, P. G., Zettl, A., Bando, H., Thess, A. & Smalley, R. E. Nanotube nanodevice. *Science* **278,** 100–103 (1997).
7. Chico, L., Crespi, V. H., Benedict, L. X., Louie, S. G. & Cohen, M. L. Pure carbon nanoscale devices: nanotube heterojunctions. *Phys. Rev. Lett.* **76,** 971–974 (1996).
8. Morales, A. & Lieber, C. M. A laser ablation method for the synthesis of crystalline semiconductor nanowires. *Science* **279,** 208–211 (1998).
9. Fonseca, A. *et al.* Synthesis of single- and multi-wall carbon nanotubes over supported catalysts. *Appl. Phys. A* **67,** 11–22 (1998).
10. Kong, J., Cassell, A. M. & Dai, H. Chemical vapor deposition of methane for single-walled carbon nanotubes. *Chem. Phys. Lett.* **292,** 567–574 (1998).
11. Dai, H., Wong, E. W. & Lieber, C. M. Probing electrical transport in nanomaterials: conductivity of individual carbon nanotubes. *Science* **272,** 523–526 (1996).
12. Rhoderick, E. H. *Metal–Semiconductor Contacts* (Clarendon, Oxford, 1978).
13. Dai, H., Hafner, J. H., Rinzler, A. G., Colbert, D. T. & Smalley, R. E. Nanotubes as nanoprobes in scanning probe microscopy. *Nature* **384,** 147–150 (1996).
14. Givargizov, E. I. in *Current Topics in Materials Science* (Kaldis, E. ed.) Vol. V1, 79–145 (North-Holland, New York, 1978).
15. Rao, K. S. R. K., Kumar, V., Premachandran, S. K. & Raghunath, K. P. Relationship of the gold related donor and acceptor levels in silicon. *J. Appl. Phys.* **69,** 2714–2716 (1991).
16. Frank, S., Poncharal, P., Wang, Z. L. & de Heer, W. A. Carbon nanotube quantum resistors. *Science* **280,** 1744–1746 (1998).
17. McCafferty, P. G., Sellai, A., Dawson, P. & Elabd, H. Barrier characteristics of PtSi/p-Si Schottky diodes as determined from I–V–T measurements. *Solid-State Electron.* **39,** 583–592 (1996).
18. Ebbesen, T. W. & Ajayan, P. M. Large-scale synthesis of carbon nanotubes. *Nature* **358,** 220–222 (1992).

Acknowledgements. We thank P. Kim and J. L. Huang for helpful discussions, and H. Wu and T. Deng for the Au electroplating solution. C.M.L. acknowledges support of this work by the ONR and NSF.

Correspondence and requests for materials should be addressed to C.M.L. (e-mail: cml@cmliris.harvard.edu).

Stress-induced recrystallization of a protein crystal by electron irradiation

F. Zemlin*, R. Schuster*, E. Beckmann*, J. L. Carrascosa†, J. M. Valpuesta† & G. Ertl*

** Fritz-Haber-Institut der Max-Planck-Gesellschaft, Faradayweg 4-6, D-14195 Berlin, Germany*

† Centro National de Biotecnologia, CSIC, Universidad Autónoma de Madrid, Cantoblanco, E-28049 Madrid, Spain

Ordering of a system of particles into its thermodynamically stable state usually proceeds by thermally activated mass transport of its constituents. Particularly at low temperature, the activation barrier often hinders equilibration—this is what prevents a glass from crystallizing[1] and a pile of sand from flattening under gravity. But if the driving force for mass transport (that is, the excesss energy of the system) is increased, the activation barrier can be overcome and structural changes are initiated[2]. Here we report the reordering of radiation-damaged protein crystals under conditions where transport is initiated by stress rather than by thermal activation. After accumulating a certain density of radiation-induced defects during observation by transmission electron microscopy, the distorted crystal recrystallizes. The reordering is induced by stress caused by the defects at temperatures that are low enough to suppress diffusive mass transport. We propose that this defect-induced reordering might be a general phenomenon.

The protein structures we investigated were well-ordered crystals of the connector protein of the bacteriophage Φ29 (ref. 3). Crystals with a thickness of several monolayers and lateral dimensions of several micrometres were prepared as described in ref. 4. These